Journal of Materials Chemistry C

PAPER

View Article Online
View Journal | View Issue

Cite this: J. Mater. Chem. C, 2015, 3, 7203

Complex physical properties of EuMgSi – a complementary study by neutron powder diffraction and ^{151}Eu Mössbauer spectroscopy

O. Niehaus,[a] D. H. Ryan,[b] R. Flacau,[c] P. Lemoine,[d] D. Chernyshov,[e] V. Svitlyk,[e] E. Cuervo-Reyes,[fg] A. Slabon,[f] R. Nesper,[f] I. Schellenberg[a] and R. Pöttgen*[a]

X-ray pure samples of EuMgSi were synthesized by reactions of the elements in sealed niobium tubes using a high frequency and subsequently a resistance furnace. The structure was investigated by single crystal X-ray diffraction: TiNiSi-type, *Pnma*, a = 769.5(2), b = 455.0(1), c = 836.9(2) pm, wR_2 = 0.033 [$I \geq 2\sigma(I)$], and 705 F^2 values with 20 variables. Powder synchrotron radiation diffraction experiments did not reveal any structural changes down to 4.3 K. Magnetic susceptibility data and ^{151}Eu Mössbauer spectra clearly indicate a stable Eu^{2+} configuration. Two distinct magnetic anomalies around 12 and 14 K can be observed for different samples with dc- and ac-susceptibility, heat capacity and resistivity measurements. Fitting of hyperfine field splitting as a function of temperature (^{151}Eu Mössbauer spectroscopy data) with a Brillouin function also leads to a magnetic ordering around 14 K. Electronic structure calculations in coincidence with the resistivity measurement prove narrow (or nearly zero) gap-semiconducting behaviour. The calculated band gap energy of 0.03 eV should be considered with precautions due to the accuracy of this method. An incommensurate magnetic structure with the propagation vector k = [$q_x \approx 0.37$, 0, 0] was determined using neutron diffraction data at 5.5 K. In consensus of dc- and ac-susceptibility and neutron powder diffraction a complex combination of antiferromagnetic and ferromagnetic interactions, most likely by super-exchange, is confirmed. These cause two magnetic ordering temperatures, though only one independent crystallographic Eu site in terms of the crystal structure is present in EuMgSi.

Received 11th April 2015,
Accepted 6th June 2015

DOI: 10.1039/c5tc01017a

www.rsc.org/MaterialsC

Introduction

Alkaline earth (AE) elements form silicides AE_2Si, which are Zintl phases with isolated Si^{4-} ions, *i.e.* they show no Si–Si bonding. The structures of AE_2Si silicides change as a function of the AE^{2+} radius. Mg_2Si[1] crystallizes into an anti-fluorite type structure where each silicide anion has cubic magnesium coordination. Ca_2Si,[2] Sr_2Si,[3] and Ba_2Si[4] adopt the orthorhombic Co_2Si structure. Silicide anions are coordinated by nine atoms in the form of a tri-capped trigonal alkaline earth prism. Although these binaries have been known for a long time, their semiconducting and only recently, their thermoelectric behaviour have been studied in detail.[5–10]

The rare earth-based silicides Eu_2Si[11] and Yb_2Si[12] are isotypic with the heavy alkaline earth silicides and they comprise two crystallographically independent rare earth sites. Yb_2Si contains diamagnetic Yb^{2+} ([Xe]4f^{14}), similar to the alkaline earth phases, while Eu_2Si is paramagnetic with Eu^{2+} ([Xe]4f^7). This offers an interesting opportunity to search for ternary silicides with an ordering of alkaline earth and rare earth cations.

So far, the ternary silicides CaMgSi,[13–17] SrMgSi,[15] BaMgSi,[15] EuMgSi,[18] and YbMgSi[18] have been reported, which belong to different structure types. The difference in the AE^{2+} radii pushes BaMgSi to the tetragonal anti-PbFCl type. Most property investigations were published for CaMgSi, which frequently occurs as a precipitate in many steels; also its hydrogenation behavior,[16] thermoelectric properties[19] and potential use as a biodegradable implant material[20] were reported.

[a] Institut für Anorganische und Analytische Chemie, Universität Münster, Corrensstrasse 30, D-48149 Münster, Germany. E-mail: pottgen@uni-muenster.de; Fax: +49-251-83-36002
[b] Physics Department and Centre for the Physics of Materials, McGill University, 3600 University Street, Montreal, Quebec H3A 2T8, Canada
[c] Canadian Neutron Beam Centre, Chalk River Laboratories, Chalk River, ON K0J 1J0, Canada
[d] Institut des Sciences Chimiques de Rennes, UMR-CNRS 6226, 263 Avenue du Général Leclerc, CS 74205, 35042 Rennes, France
[e] European Synchrotron Radiation Facility, 6 Rue Jules Horowitz, BP 220, Grenoble, France
[f] Department of Chemistry and Applied Biosciences, ETH Zürich, Vladimir-Prelog-Weg 1, CH-8093 Zürich, Switzerland
[g] Reliability Science and Technology, EMPA Dübendorf, Überlandstrasse 129, CH-8600 Dübendorf, Switzerland

In the course of our systematic studies on equiatomic europium intermetallics (ref. 21–24, and references therein) we were interested in the magnetic behaviour of EuMgSi, as a continuation of our recent studies on isotypic EuMgGe.[25] Herein we report on the synthesis, structural characterization, chemical bonding, the magnetic structure, and transport properties of EuMgSi along with a detailed ^{151}Eu Mössbauer spectroscopic characterization, which lead to a deeper understanding of the structure–property relationships. One major impact of the present study concerns the determination of the europium magnetic structure using a flat-sample technique, overcoming the difficulties that result from the large neutron absorption.[26]

Experimental

Synthesis

Starting materials for the preparation of EuMgSi were sublimed ingots of europium (Alfa-Aesar), magnesium rods (Alfa-Aesar), and silicon lumps (Alfa-Aesar) all with stated purities better than 99.9%. The air- and moisture-sensitive europium ingots were kept in a Schlenk tube under argon prior to the reaction. The elements were weighed in the ideal 1 : 1 : 1 atomic ratio and arc-welded in niobium tubes under 800 mbar argon. Argon was purified over titanium sponge at 873 K, silica gel, and molecular sieves. Niobium ampoules were subsequently placed in a water-cooled sample chamber of an induction furnace (Hüttinger Elektronik, Freiburg, Germany, Typ TIG 1.5/300).[27] The elements were prereacted at 1400 K for 5 min and heated for 2 h at 1000–1150 K, followed by quenching. The temperature was controlled using a Sensor Therm Methis MS09 pyrometer with an accuracy of ±30 K. Thereafter, the niobium ampoules were sealed in silica tubes under vacuum and heated at 1300 K for 12 hours and then slowly cooled down within 10 days in order to achieve a better crystallinity of the product. No reaction with the container material was observed. The polycrystalline samples show silvery-metallic lustre and no significant air- or moisture-sensitivity.

Laboratory X-ray and synchrotron powder diffraction

The polycrystalline samples of EuMgSi were characterized using Guinier powder patterns (Cu $K_{\alpha 1}$ radiation, α-quartz: a = 491.30, c = 540.46 pm as internal standard). The Guinier camera was equipped with an imaging plate technique (Fujifilm, BAS-READER 1800). The orthorhombic lattice parameters were refined using a least-squares routine. Proper indexing of diffraction lines was ensured by an intensity calculation[28] using the positional parameters obtained from the single crystal investigation. The powder and single crystal lattice parameters show good agreement with values from the literature.[18]

Irregularly shaped crystal fragments were obtained from the crushed EuMgSi sample. They were glued to small quartz fibres using beeswax and the suitability of intensity data collection was first checked by Laue photographs on a Buerger camera (white Mo radiation, image plate technique, Fujifilm, BAS-1800). A dataset was collected by using an IPDS II diffractometer (graphite monochromatized Mo K_{α} radiation; oscillation mode, and room temperature) and a numerical absorption correction was applied. All relevant crystallographic data and details of the data collection and evaluation are listed in Table 1.

Table 1 Crystal data and refinement of EuMgSi, with TiNiSi type structure, space group *Pnma* (no. 62), and Z = 4

Refined composition	EuMgSi
Molar mass/g mol^{-1}	204.4
Lattice parameters/pm	a = 769.5(2)
(Guinier powder data)	b = 455.0(1)
	c = 836.9(2)
Cell volume/nm^3	V = 0.2930
Calculated density/g cm^{-3}	4.63
Crystal size/μm^3	30 × 40 × 80
Detector distance/mm	60
Exposure time/min	4
ω-range, increment/°	0–180/1.0
Integr. param./A, B, EMS	12.0/0.3/0.010
Transmission ratio (max/min)	0.76/0.23
θ range/°	3.6–35.0
Absorption coefficient/mm^{-1}	22.0
F(000)	356
Range in hkl	±12, ±7, ±13
Total no. reflections	4456
Independent reflections/R_{int}	705/0.0313
Reflections with $I \geq 2\sigma(I)$/R_{σ}	626/0.0136
Data/parameters	75/20
Goodness-of-fit on (F^2)	1.07
R/wR for [$I \geq 2\sigma(I)$]	0.0143/0.0327
R/wR for all data	0.0180/0.0331
Extinction coefficient	417(15)
Largest diff. peak and hole/e Å^{-3}	0.84/−0.78

The temperature-dependent powder diffraction data were collected at the Swiss-Norwegian Beam Lines, BM01A station at the ESRF (Grenoble, France) using a Dectris Pilatus2M detector in a 4.3–30 K temperature range with a typical step width of 3 K at the wavelength of 0.6889 Å. The temperature was controlled using an in-house developed He blower. Experimental powder diffraction data were integrated and processed using the FIT2D software;[29] structural parameters were refined using the FullProf software.[30,31] During the refinement peak profiles were modelled using a pseudo-Voigt function and the TiNiSi type structure was used as an initial model. Only isotropic Debye–Waller factors were implemented. No additional Bragg reflections indicating deviation from the model seen in the residual curve.

EDX data

The single crystal investigated on the diffractometer was studied by semiquantitative EDX analysis using a Zeiss EVO® MA10 scanning electron microscope in variable pressure mode with EuF_3, SiO_2, and MgO as standards. The analysis at several points of the crystal is in line with the equiatomic stoichiometry within the precision of the experiment. No impurity elements (especially from the container material) were detected.

Structure refinement

In accordance with the literature[18] the X-ray diffractometer dataset showed an orthorhombic lattice and the systematic extinctions were in agreement with space group *Pnma*. The starting parameters were deduced using the Superflip algorithm[32]

Table 2 Atomic coordinates and anisotropic displacement parameters (pm^2) of EuMgSi. $U_{12} = U_{23} = 0$. U_{eq} is defined as one third of the trace of the orthogonalized U_{ij} tensor. Coefficients U_{ij} of the anisotropic displacement factor tensor of the atoms are defined by: $-2\pi^2[(ha^*)^2U_{11} + \cdots + 2hka^*b^*U_{12}]$

Atom	Wyckoff position	x	y	z	U_{11}	U_{22}	U_{33}	U_{13}	U_{eq}
Eu	4c	0.01547(2)	1/4	0.68405(2)	94(1)	97(1)	108(1)	−3(1)	99(1)
Mg	4c	0.14613(14)	1/4	0.06627(15)	100(4)	93(5)	98(5)	14(4)	97(3)
Si	4c	0.27900(11)	1/4	0.39035(11)	81(3)	71(4)	92(4)	−2(3)	81(2)

Table 3 Interatomic distances (pm), calculated using the powder lattice parameters of EuMgSi. All standard deviations are equal or less than 0.2 pm. All distances of the first coordination spheres are listed

Eu	1	Si	318.6	Si	2	Mg	277.0
	2	Si	326.5		1	Mg	284.8
	2	Si	327.1		1	Mg	289.9
	2	Mg	330.0		1	Eu	318.6
	1	Mg	335.3		2	Eu	326.5
	1	Mg	353.1		2	Eu	327.1
	2	Mg	359.6		1	Eu	400.0
	2	Eu	383.7	Mg	2	Si	277.0
	1	Si	400.0		1	Si	284.8
	2	Eu	400.3		1	Si	289.9
					2	Eu	330.0
					1	Eu	335.3
					1	Eu	353.1
					2	Eu	359.6

embedded in the Jana2006 program package.[33] The structure was refined using anisotropic displacement parameters for all atoms (full-matrix least-squares on F_o^2). As a check for the correct composition, we refined all occupancy parameters in a separate series of least-squares cycles. All sites were fully occupied within two standard deviations and in the final cycles the ideal occupancy parameters were assumed again. The final difference Fourier synthesis revealed no relevant residual peaks. Refined atomic positions, displacement parameters and interatomic distances are given in Tables 2 and 3.

Further details of the structure refinement are available at Fachinformationszentrum Karlsruhe, D-76344 Eggenstein-Leopoldshafen (Germany), by quoting the Registry No. CSD-429473.

Computational details

The electronic band structure of EuMgSi was calculated within the DFT approximation using three different implementations: CASTEP[34] and Dmol3[35] packages available in Materials Studio 5.1 as well as the TB-LMTO-ASA[36] code from the Max-Plank Institute in Stuttgart. The use of several codes was intended to verify the robustness of the results against the changes in the choice of the basis set, and ways of treating the potential of the lattice and the exchange correlation functional. For details on the differences among these implementations the reader can refer to the original literature.

The tolerance for the energy convergence of the self-consistent calculations was set to always lower than 0.1 meV. We used the PBE GGA[37] exchange correlation functional within CASTEP and the POB GGA[38] functional within DMol3. For the LMTO calculations we employed the Langreth–Mehl–Hu functional.[39] In all cases the quasi-particle states were calculated several times, increasing the resolution of the grid in reciprocal space, in order to ensure the convergence of the results. The results reported here were obtained using grids having a point spacing smaller than 0.01 $Å^{-1}$. It has been shown that the valence bands of europium containing-Zintl phases are not notably disturbed when europium is replaced by strontium.[40] In this way the bands presented have been obtained, as that avoids the cumbersome appearance of many flat f bands with no contribution to the bonding. It should be noted that magnetic ordering of electrons in f states is not well captured within the DFT approximations.

The electron localization function (ELF)[41,42] was calculated from the electronic structure within the LMTO, as implemented by A. Savin. Post-processing and graphic representation were done using a code developed in house by E. Cuervo-Reyes. The plots contain information of both ELF and electron density over a given plane. ELF values and electron density values are shown as the colour of the pixels and the number of coloured pixels, respectively, over a black background.

Physical properties

Magnetic susceptibility, heat capacity as well as the electrical resistivity investigations have been performed using a Quantum Design Physical-Property-Measurement-System (PPMS) using the VSM-(Vibrating Sample Magnetometer), ACMS, ac-transport and the heat capacity option, respectively.

For the VSM measurements, 24.749 mg of the powdered sample was packed in a polypropylene capsule and attached to the sample holder rod. The sample was investigated in the temperature range of 2.5–305 K and with magnetic flux densities up to 80 kOe.

For ac-MS measurements, 48.138 mg of the powdered EuMgSi sample was enclosed in a thin-walled gelatine capsule. These investigations were performed in the temperature range of 6–20 K with internal frequencies from 11 to 9999 Hz and different magnetic field strengths up to 20 kOe.

A 1.5 mm thick tablet of EuMgSi was sintered for 20 days and then used for the resistivity measurement, which was carried out using the van-der-Pauw technique.[43] The ACT puck was modified using a press contact assembly purchased from Wimbush Science & Technology. Probes are spring contacts, gold plated over nickel and the distance between the pins was set to 2 mm. The resistivity was measured between 2.5 and 300 K at 0 and 1000 Oe. The recorded data of channels 1 & 2 were converted according to the van-der-Pauw equation given in the Quantum Design Application Note 1076-304. To check the accuracy of our determined specific resistivity we have measured a gold tablet (thickness: 1.45 mm) using the same assembly in comparison. In the whole temperature range we observed almost the same deviation. At 293 K a

value of 1.73 × 10^{-6} Ω cm could be obtained, while in the literature a value of 2.21 × 10^{-6} Ω cm is reported.[44]

Heat capacity was measured using 4.329 mg of the crushed sample, which was fixed to a pre-calibrated heat capacity puck using Apiezon N grease and investigated between 2.5 and 310 K.

^{151}Eu Mössbauer spectroscopy

The 21.53 keV transition of ^{151}Eu with an activity of 130 MBq (2% of the total activity of a ^{151}Sm:EuF_3 source) was used for the Mössbauer spectroscopic experiment, which was conducted in the usual transmission geometry. The temperature of the absorber was varied using a commercial helium-flow cryostat, while the source was kept at room temperature. The sample was enclosed in a small PMMA container at a thickness corresponding to about 10 mg Eu cm^{-2}. Initial fitting of the spectra was performed using the Normos-90 program system.[45] These fits were supplemented using a model that included the possibility of an incommensurate modulation of the moments above 8 K.[46]

Neutron diffraction

Powder neutron diffraction measurements were made at a wavelength of 1.3286(2) Å using a large-area flat-plate mount[26] to reduce the impact of the large absorption cross-section of natural europium. Additional measurements were also made at a wavelength of 2.3696(2) Å to confirm that no low-angle diffraction peaks had been missed by working at 1.3286(2) Å. The sample was powdered in a helium-filled glove-box and immobilised on the single-crystal silicon plate using diluted (1%) GE-3070 varnish. The plate was mounted under 1 atm. of helium in an indium-sealed aluminium can to protect it from oxidation.

The neutron diffraction patterns were collected on the 800-wire C2 powder diffractometer at the Canadian Neutron Beam Centre, Chalk River, Ontario, using a closed-cycle helium refrigerator to cool the sample.

Analysis of neutron patterns were performed by Rietveld profile refinement using the FULLPROF software.[30,31] No absorption correction was applied, however, the neutron data recorded at 1.3286 Å were truncated at 2θ = 62° in order to reduce the impact of absorption effects.

Results and discussion

Crystal chemistry

Like already known from the literature EuMgSi crystallizes in the quite common TiNiSi type structure,[18] which has repeatedly been reviewed in the literature, emphasizing the structural relationship with the aristotype AlB_2. In this part we will discuss only some distinct points of the structure; for further details we can refer to the literature.[47–51]

In general, compounds exhibiting the TiNiSi-type structure are described with a three-dimensional infinite (covalently bonded) polyanionic network which corresponds to the puckered and orthorhombically distorted hexagons of the aristotype AlB_2.[47] Instead of titanium and nickel in the prototype, in EuMgSi the significantly more electropositive europium and magnesium

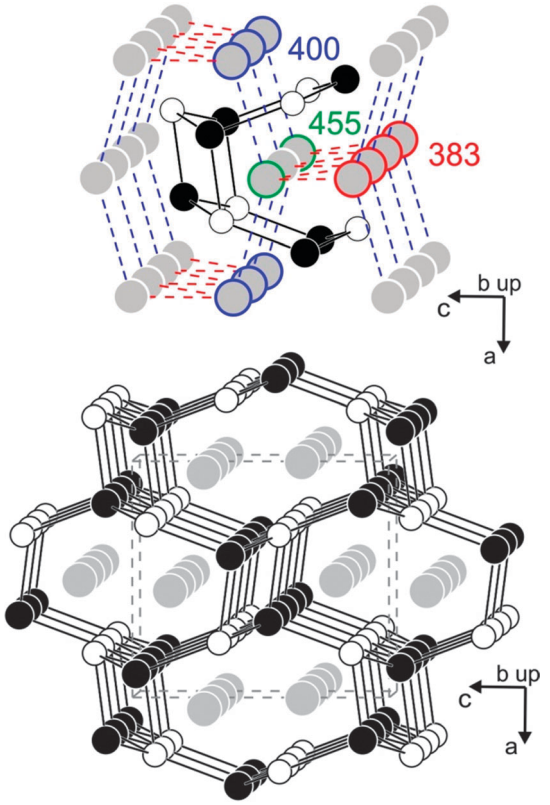

Fig. 1 The crystal structure of EuMgSi: europium, magnesium, and silicon atoms are indicated as dark grey, black filled and open circles, respectively. The top panel shows the coordination sphere of europium plus the 3D europium network. Relevant Eu–Eu distances are highlighted in different colours. In the bottom panel the typical network of Mg and Si for the TiNiSi-type structure is emphasized, while europium is placed in the cavities.

atoms occupy these crystallographic sites. Now the corrugated network is formed by the magnesium and silicon atoms.

EuMgSi can also be described as a Zintl-phase $(Eu^{2+})(Mg^{2+})(Si^{4-})$. Nevertheless, in the bottom part of Fig. 1 a polyanionic [MgSi] network is emphasized. In this network each magnesium atom has a distorted tetrahedral $MgSi_{4/4}$ coordination of silicon atoms and *vice versa*. These tetrahedra are linked *via* common edges and corners, forming the three-dimensional polyanionic network in which the europium atoms occupy channels along the *b* axis. The Mg–Si distances range between 277 and 290 pm which is somewhat larger than the sum of the covalent radii of 253 pm.[52] Taking the ionic radii for Si^{4-} (271 pm) and Mg^{2+} (79 pm)[52] into account, it is unambiguous that the bonding situation is somewhere between the covalent and the ionic model. This is totally in line with the theoretical calculations (*vide infra*).

The europium atoms have a near-neighbour environment of two tilted and puckered hexagons of Mg and Si atoms, resulting in a coordination number (CN) of 12. The Eu–Eu distances within the channels along *b* are somewhat longer (455 pm) than between different channels (383 and 400 pm). Consequently, the Eu substructure can be described as two zig-zag chains along the *a* (400 pm) and *b*-axis (383 pm), which will be important for the discussion of the magnetic structure (*vide infra*).

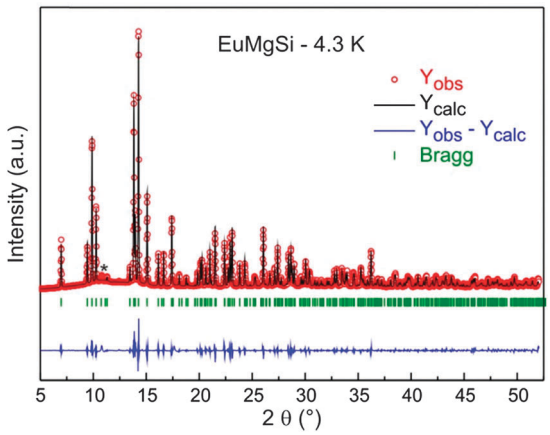

Fig. 2 Synchrotron (λ = 0.6889 Å) powder pattern (red) of EuMgSi at 4.3 K with Rietveld-fit (black), Bragg positions (green) and difference curve (blue). The reflection marked by an asterisk is caused by icing.

In order to investigate the influence of the observed magnetic anomalies on the structure, powder synchrotron measurements have been performed in the temperature range of 4.3 to 30 K. In Fig. 2 data for 4.3 K and the corresponding Rietveld refinement is shown. For all investigated temperatures no deviations from the TiNiSi type structure and no significant anomalies in the lattice parameters were observed.

Electronic structure and chemical bonding

Atomic coordination and electron counting suggest that the formal charge partitioning $Eu^{2+}Mg^{2+}Si^{4-}$ is the most reasonable one for EuMgSi, as is also observed for all binary M_2Si compounds with divalent metals (M). There is no Si–Si contact within normal bonding distances, and europium ions in Zintl compounds have been so far found in a divalent state. However, whether the system is actually a metal or a semiconductor depends on the details of the band structure and cannot be guessed in an *a priori* way. It has been shown for other ternary and quaternary Zintl phases that the dispersion of valence bands due to the ecliptic stacking of the Zintl anions causes an overlap of some valence bands with the otherwise empty conduction bands. The band structure of EuMgSi within the DFT approximation is shown in Fig. 3. For the sake of clarity we

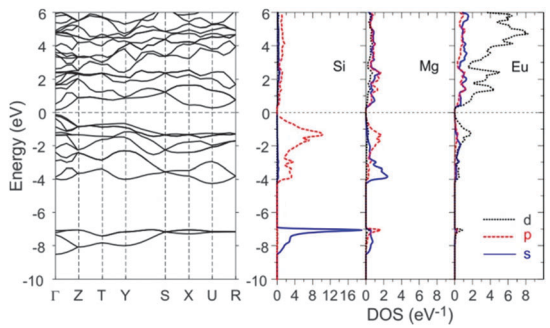

Fig. 3 Electronic band structure of EuMgSi in the DFT approximation (left) and the density of states (DOS) of all atoms (right). Europium atoms were replaced by strontium ones in the calculation.

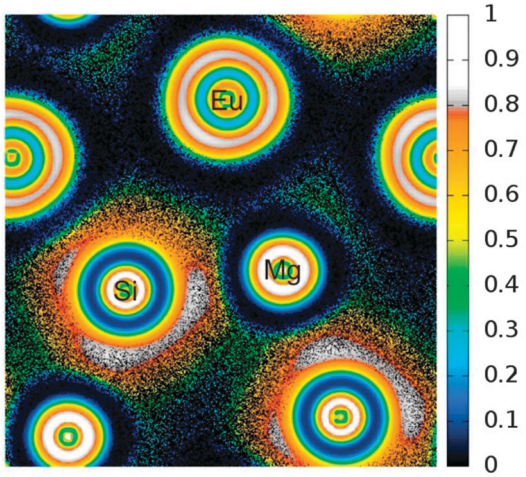

Fig. 4 Planar cut of the electron localization function (ELF) in the *ac* plane at y = 0.25b. The different anions and cations are labelled. The polarization of the silicon anions toward Mg-cations is clearly visible, indicating a partially covalent interaction, and in contrast to the more cationic role of europium.

left the core states out of the picture. With four formula units per primitive cell, there are four deep bands with dominant contribution from Si-3s states, and 12 bands from Si-3p states between −4 eV and the Fermi level. The highest valence band shows a significant dispersion in the S–Y segment in reciprocal space, as a consequence of the abovementioned stacking along the b axis. Yet, a nearly zero gap remains between this band and the first conduction band, providing the system with a small gap-semiconductor. This gap is a direct one at the gamma point. Although DFT does not always provide a good representation of electronic states around the Fermi level, the tendency is always to close the gap. Therefore, we have reasons to believe the existence of a small direct gap in the present case.

The projection of the density of states onto atomic orbitals gives evidence of the different roles played by Eu and Mg (Fig. 3). The larger contribution to the occupied DOS from the latter, right at the energies where the Si-p states are, evidences the partially covalent interaction with silicon. Some mixing of Mg with the Si-s states can be identified, whereas Eu acts more like a cation. This view is supported by the electron localization function (ELF). The surface cut presented in Fig. 4 shows the polarization of the isolated Si shell towards Mg. Thus, both the band structure and the ELF suggest describing EuMgSi as a typical Zintl phase with partially covalent character.

Magnetic properties and heat capacity

The temperature dependent magnetic and inverse magnetic susceptibility (χ and χ^{-1} data) of EuMgSi measured in an external field of 10 kOe is displayed in the top panel of Fig. 5. A fit of the χ^{-1} data in the region of 50–300 K using the Curie–Weiss law, revealed an effective magnetic moment of μ_{eff} = 7.97(1) μ_B per Eu atom and a Weiss constant of θ_p = 14.5(5) K. The effective magnetic moment is almost identical to the theoretical value of 7.94 μ_B for a free Eu^{2+}-ion, proving clearly the divalent character of europium. The Weiss constant is proportional to the sum of all

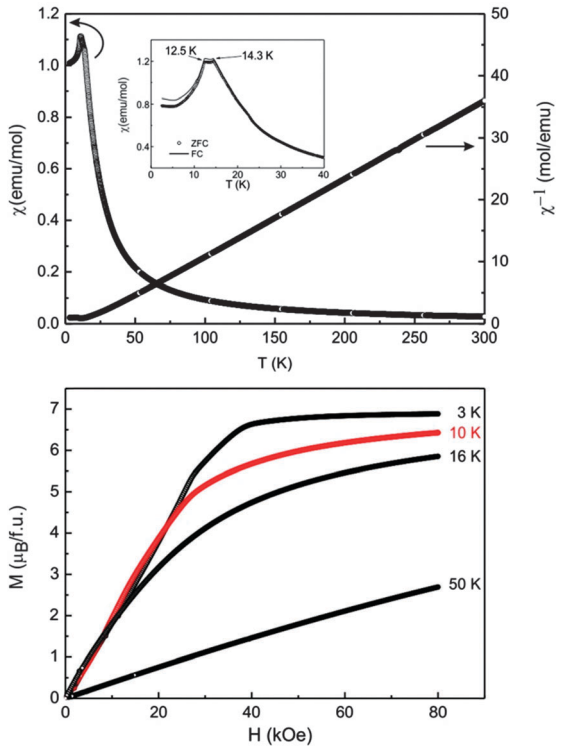

Fig. 5 Magnetic properties of EuMgSi (dc susceptibility): (top) temperature dependence of the magnetic susceptibility χ and its reciprocal χ^{-1} measured with a magnetic field strength of 10 kOe. The inset shows the magnetic susceptibility in zero-field (ZFC) and field-cooled (FC) modes at 100 Oe; and (bottom) magnetization isotherms at 3, 10, 16 and 50 K.

(pair-wise) exchange couplings experienced by a magnetic center. Therefore, the positive value of the Weiss constant indicates a majority of ferromagnetic couplings. The susceptibility data show two distinct anomalies slightly above 10 K.

To obtain more precise information about these orderings, a low-field measurement (100 Oe) was performed in a zero-field- and field-cooled mode (ZFC/FC), which is shown in the inset of Fig. 5. Two well separated anomalies can be observed for EuMgSi at $T_N(1)$ = 14.3(3) K and $T_N(2)$ = 12.5(3) K. Below the second magnetic transition an obvious decrease of the magnetic susceptibility can be observed. Such behaviour is usually attributed to an antiferromagnetic character. In general, positive Weiss constants do not necessarily exclude antiferromagnetic orderings. Very prominent examples from the literature for such a case are the iron and cobalt halides $FeCl_2$, $FeBr_2$, $CoCl_2$ and $CoBr_2$. They crystallize in the well-known $CdCl_2$-type structure, in which the transition metals form ferromagnetic sheets, while the moments in adjacent layers are oriented antiparallel. Despite the antiferromagnetic spin structure, most of the pair-wise (in-plane) interactions are ferromagnetic.[53]

One particularity that should be mentioned is a weak bifurcation between the ZFC- and FC-curves, which can only take place if the system shows a non-zero remanent magnetization. This might be intrinsic or due to a minor impurity phase, but it is certainly not compatible with a simple antiferromagnetic ordering. A second, more significant observation is the presence of two distinct anomalies, while only one crystallographically independent Eu site is present in this structure referring to X-ray experiments. Consequently, it is impossible to classify the observed anomalies as ferro- or antiferromagnetic just referring to susceptibility measurements. A very important point in this case is to clarify that both anomalies have intrinsic characters. Further investigations like heat capacity or ^{151}Eu Mössbauer spectroscopy (*vide infra*) as well as repeated measurements on different samples prove unambiguously intrinsic behaviour. Furthermore, two distinct anomalies are also reported for the isotypic compounds EuMgGe[25] and EuMgSn.[54] In contrast to Ma *et al.* we do not believe that the ordering temperature depends significantly on the orientation of the crystals and causes the observed two anomalies.[54] If this would be the case, only one broad singularity would be visible in the temperature dependence of the specific heat in the absence of an external magnetic field for a powdered sample.

Additionally magnetization measurements at certain temperatures (3, 10, 16 and 50 K) were performed for EuMgSi. These are shown in the bottom panel of Fig. 5. The isotherms at 3 and 10 K exhibit a slightly s-shaped character, which can be attributed to a weak field induced spin-reorientation. These can be observed for the 3 and 10 K isotherms at 17(3) and 10(2) kOe, respectively. Clearly, this behaviour proves a somehow opposite orientation of the spins which can be reoriented already at small magnetic fields. However, the differences between the two magnetic ordering temperatures are too small to investigate possible differences between these by magnetization isotherms. One peculiarity, which should be mentioned, is the unusual linear increase of the magnetization subsequent to the spin-reorientation for the 3 K isotherm of EuMgSi. Only at higher external field strength the typical curvature due to saturation occurs and leads to a magnetic moment of 6.9(1) μ_B per Eu atom at 80 kOe. This corresponds almost to the expected saturation magnetization of 7.0 μ_B according to $g_J \times J$. Finally, it should be mentioned that all isotherms are measured as hysteresis loops, but no hysteresis that could indicate global ferromagnetic ordering (with remanent magnetization) is observed.

To confirm our suggestion of two intrinsic magnetic anomalies, heat capacity measurements were performed without an external field in the temperature range of 2.5–300 K. The resulting data are displayed in Fig. 6 and confirm the presence of two anomalies at 11.9(2) and 14.2(2) K. The observed temperatures are in excellent accordance with the temperatures determined from the susceptibility data. The higher-T anomaly looks like a λ-transition, as it would be expected for a second order magnetic ordering, which is not coupled to a lattice distortion (the latter would make it first order). The lower-T transition exhibits almost the same form indicating also a second order transition and might result from a reorientation of a part of the magnetic structure.

For a better understanding of this complex magnetic behaviour and especially in order to investigate if any dynamic processes take part, ac-MS measurements have been performed. The zero field in-phase susceptibilities $\chi'(\omega, T)$ are depicted for a number of frequencies in Fig. 7. As described above two

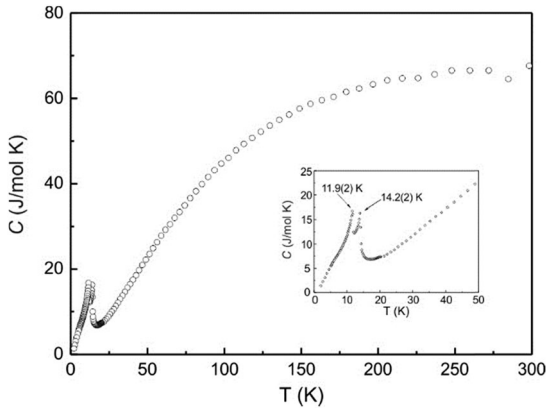

Fig. 6 Heat capacity of EuMgSi measured in the temperature range of 2.5 to 305 K without an applied field. The inset shows the magnified low-temperature area to highlight the two anomalies.

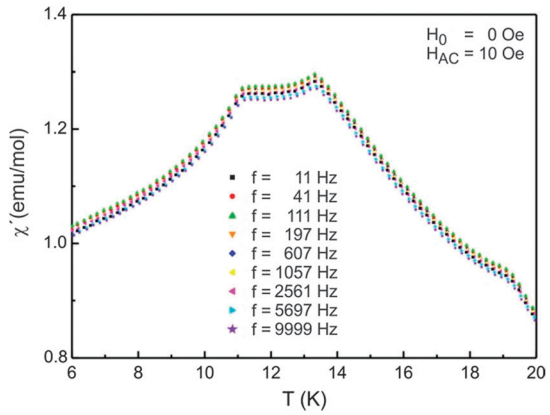

Fig. 7 Magnetic properties of EuMgSi (ac susceptibility): temperature dependence of the magnetic susceptibility $\chi'(\omega)$ recorded after (ZFC) with internal frequencies ranging from 11 to 9999 Hz.

anomalies at 13.3(1) and 11.1(1) K are clearly visible. No obvious frequency-dependent behaviour and no shift of the anomalies to higher temperatures with decreasing frequencies is observed as found for spin-glasses.[55] Furthermore the out-of-phase susceptibilities $\chi''(\omega, T)$ (not shown here) are almost zero for all frequencies and are independent of H_{Ac} confirming that no dynamic processes take place. Fig. 8 displays the influence of external dc magnetic fields up to 20 kOe on $\chi'(\omega = 197\ \text{Hz}, T)$. Again no temperature dependency of the out-of-phase $\chi''(\omega, T)$ is detectable, reasoning why these data are not shown here. The field dependency of ac-MS was measured after ZFC with increasing temperature and afterwards the measurements were continued with decreasing temperatures. Only less irreversibility could be detected for the measurements with H_0 = 0.5 and 1 kOe. It is a little bit conspicuous that the highest absolute χ' values are observed for the measurement with an external field strength of 1 kOe; however, a similar behaviour has already been described for NdRhSn.[56] It could be shown that an increase of the field strength shifts $T_N(2)$ to minimal lower temperatures, while $T_N(1)$ is constant up to 1 kOe. However, the 5 kOe curve shows a small shift to a lower temperature. Such a

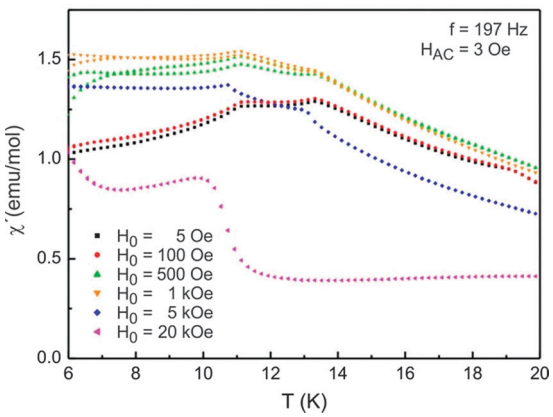

Fig. 8 Magnetic properties of EuMgSi (ac susceptibility): temperature dependence of the magnetic susceptibility $\chi'(\omega)$ measured after ZFC with increasing temperature and back in the FC process (with decreasing temperature from the paramagnetic state) at different magnetic field strengths up to 20 kOe at a constant frequency of f = 197 Hz.

development is often explained by the special nature of antiferromagnetic transitions. An external magnetic field creates a force that counteracts with the antiferromagnetic exchange interactions, driving the Néel temperature to lower temperatures.[57] However, we do not want to state an antiferromagnetic ordering for EuMgSi, and we just like to show that some characteristics of this complex magnetic behaviour indicate at least some opposite spin orientations. At H_0 = 20 kOe a very small maximum is recognized at 9.9(2) K followed by a clear decay. The inflection point has been determined at 10.7(1) K. The data for 20 kOe are characteristic for ferromagnetic-like transitions.[58] Consequently, only one transition is observed because the spins exhibit already parallel orientation. This behaviour is perfectly in line with the 3 and 10 K magnetization isotherms that exhibit spin reorientations already below 20 kOe (*vide supra*).

Electronic properties

Fig. 9 shows the electrical resistivity of EuMgSi as a function of temperature without an applied field. At an applied field of 1000 Oe no magnetoresistance is observed (not shown here). As illustrated in the inset, also the electrical resistivity exhibits two distinct anomalies in the temperature range of the other methods. Below the second anomaly a significant drop is observed due to less scattering of the conduction electrons. A second important feature is the conductivity behaviour above the ordering temperatures. Note that in the present case, the resistance decreases with temperature, as observed in a semiconductor, but the trend is very weak. Although the temperature is varied over two orders of magnitude, the resistivity only drops to one half of its maximum value. It should also be noted that the resistivity is much smaller than that typically found for semiconductors with values similar to those of amorphous carbon. Employing the Arrhenius equation $\rho = \rho_0 \exp(\Delta/kT)$, where ρ_0 is a pre-exponential factor, Δ is the activation energy and k is the Boltzmann constant, the calculated band gap energy E_g corresponds to approximately two times the activation

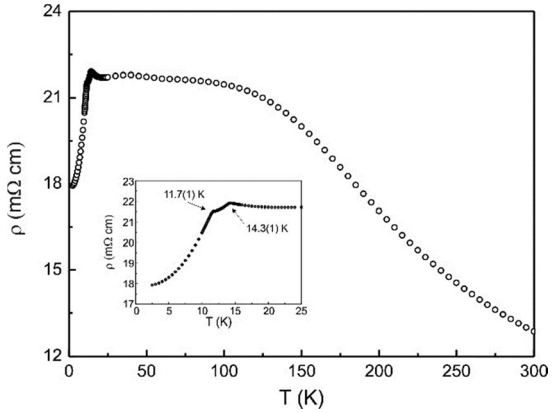

Fig. 9 Temperature dependent electrical resistivity ρ of EuMgSi. The inset shows the magnified low-temperature area to highlight the two anomalies and the significant drop below the second anomaly.

energy Δ.[59,60] As a consequence the slope of a linear fit is $E_g/2k$ and a bandgap of approximately 0.03 eV could be calculated. It should be mentioned that the values of experimentally determined band gap energies are, in general, too small due to impurity states within the band gap. However, this measurement clearly confirms the nearly zero gap-semiconducting nature of EuMgSi as was predicted by DFT calculations (*vide supra*).

^{151}Eu Mössbauer spectroscopy

Experimental and simulated ^{151}Eu Mössbauer spectra of EuMgSi are presented in Fig. 10. All temperatures show a major resonance with an isomer shift ranging between $-10.47(6)$ mm s^{-1} (11.4 K) and $-10.16(1)$ mm s^{-1} (4.2 K) indicating stable divalent europium. A minor resonance at an isomer shift around 1 mm s^{-1} represents extrinsic Eu^{3+} most likely formed during grinding due to surface oxidation. The Eu^{2+} resonance is a singlet well above and a split signal below the ordering temperature due to Zeeman splitting. Temperature dependent measurements on EuMgSi illustrate a beginning of magnetic hyperfine field splitting at 14.2 K, which results in a clear splitting with decreasing temperature (Fig. 10). A Brillouin function fit calculated with $S = 7/2$ for the Eu^{2+} cation describes the temperature dependence of the measured magnetic hyperfine field well (Fig. 11). The obtained intersection crossings give an estimated ordering temperature of 13.5(1) K, rather lower than that derived above using bulk measurements. The value of the saturated magnetic hyperfine field is B_{sat} = 22.5(1) T. The isomer shift and hyperfine field values are consistent with several other equiatomic europium intermetallics.[11,23]

While the fits to the spectra appear reasonable, closer inspection reveals that they require a marked increase in linewidth above 8 K (Fig. 12) that clearly reflects behaviour that is being missed by assuming a single unique environment for the europium ions in EuMgSi as T_N is approached from below. As there is only a single crystallographic site occupied by europium, and given the complex helimagnetic structure deduced from the neutron diffraction data discussed below, we considered the possibility that the changes in the spectral shape may be due to the development of an incommensurate modulation of the europium moments, as reported previously in $EuNiGe_3$,[46] EuPdSn,[61] and Eu_4PdMg.[62] Fitting with a distribution constructed from a constant offset plus an incommensurate, one-term sinusoidal modulation (spectra are presented in Fig. 13) yielded improved fits and reduced (but did not fully eliminate) the excursion in linewidth between 8 K and T_N (Fig. 12). The temperature dependence of the average hyperfine field yields a slightly higher transition temperature of 14.3(1) K (Fig. 14), fully consistent with the values determined above using low-field dc susceptibility (Fig. 5) and heat capacity (Fig. 6), while the magnitude of the sinusoidal modulation term ($B_k(1)$) provides some evidence for a second transition between 8 K and 10 K where the shape of the spectra clearly changes (Fig. 13).

Neutron diffraction

The neutron diffraction data recorded in the paramagnetic state (T = 20 K) and in the magnetically ordered state (T = 5.5 K) at a wavelength of λ = 1.3286 Å are presented in Fig. 15. The neutron diffraction pattern recorded at 20 K shows the nuclear diffraction peaks of the TiNiSi-type EuMgSi compound. The XRD pattern observed after neutron measurements did not provide any evidence of impurity phases in the sample, and thus, the extra peaks observed in the neutron diffraction pattern (2Θ = 34.6°, 36.6°, 40.1°, and 53.1°) can be attributed to the sample holder environment. The neutron diffraction pattern recorded at 5.5 K includes many new purely magnetic diffraction peaks. These can be indexed to the propagation vector $k = [q_x \approx 0.37, 0, 0]$ indicating an incommensurate magnetic structure. The absence of magnetic contributions to the nuclear peaks allows us to exclude any ferromagnetic contribution, and the absence of higher order harmonic peaks allows us to exclude a square-modulated magnetic structure. Refinements carried out with a sine wave modulated magnetic structure lead to bad fits, while refinements carried out with a helimagnetic structure yield good quality fits and refined R-factors. The absence of lower angle magnetic diffraction peaks was confirmed by neutron diffraction patterns recorded at 20 K and 5.5 K using a wavelength of 2.3696 Å. No magnetic peaks were found below the $(000)^{+/-}$ peak shown in Fig. 15. Fitting the temperature dependence of this strong magnetic peak to a squared Brillouin function yields an ordering temperature of 14.3(1) K, in perfect agreement with that derived from the average hyperfine field.

Considering a helimagnetic structure, the best refinement is obtained with magnetic moments oriented in the (b, c) plane and magnetic phases of 0, 0, 0, and 0 for the Eu atoms with positions (x, 1/4, z), ($-x$, 3/4, $-z$), (1/2 − x, 3/4, 1/2 + z), and (1/2 + x, 1/4, 1/2 − z), respectively. However, this planar helimagnetic structure leads to magnetic structural factors of zero intensity for the ($0kl$) diffraction peaks with $k + l = 2n + 1$, while $(001)^{+/-}$ and $(010)^{+/-}$ magnetic peaks are experimentally observed (in the inset of Fig. 15). This points to a refinable magnetic phase angle. Moreover, the ($hk0$) diffraction peaks with $h = 2n + 1$ are absent, suggesting that the translation mode a is conserved. This demands identical magnetic phase angles for the Eu atoms related to the a glide plane (*i.e.* between Eu(1)

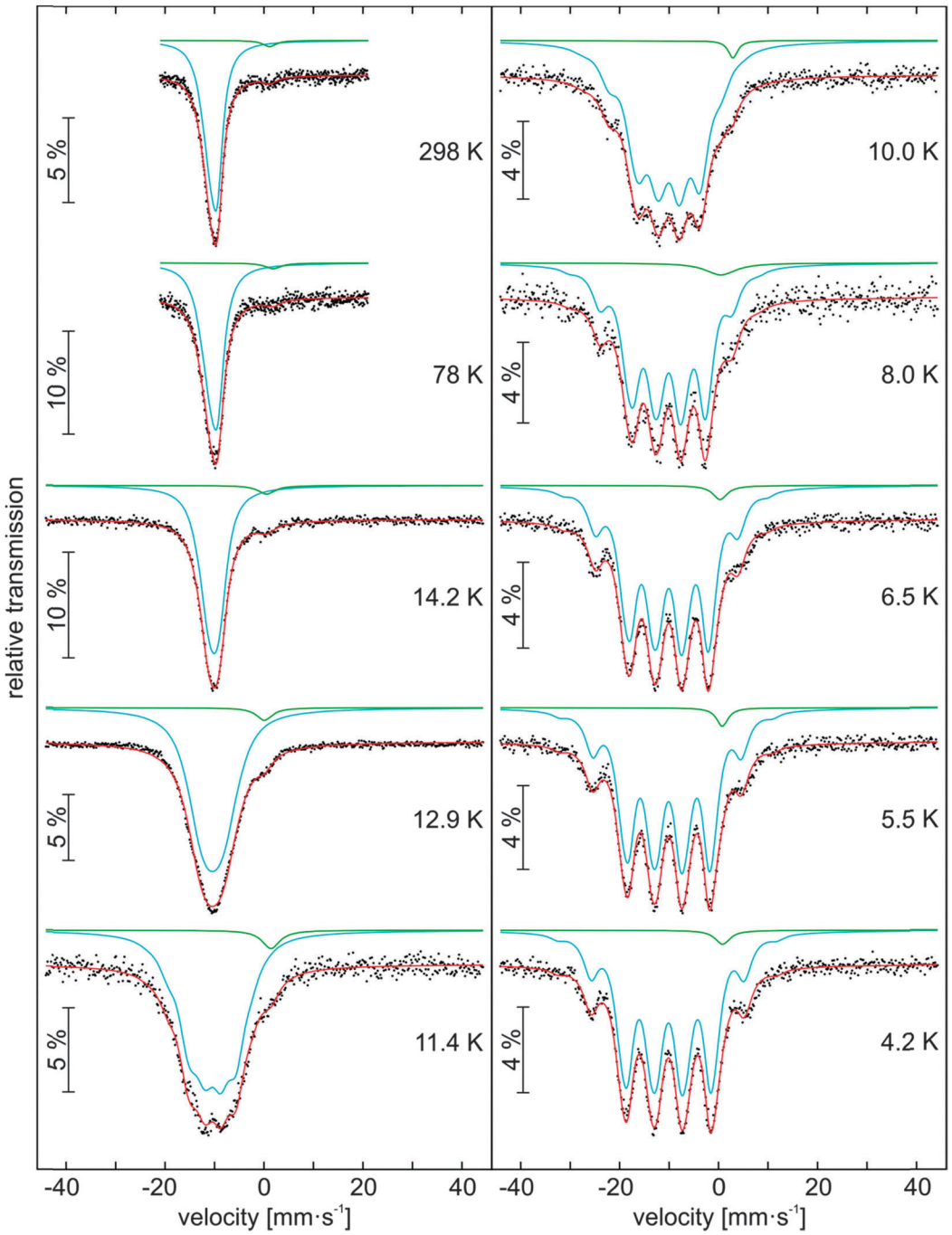

Fig. 10 Experimental (black dots) and simulated (red line) ^{151}Eu Mössbauer spectra of EuMgSi at certain temperatures.

and Eu(4), and between Eu(2) and Eu(3)). For the numbering of Eu atoms we refer to Fig. 16. Thus, the refinement can be improved by considering a weak magnetic phase angle of 0.09(1) for Eu(2) and Eu(3) atoms, while the magnetic phase angle of Eu(1) and Eu(4) atoms is kept zero (Fig. 15). The refined parameters of the 5.5 K neutron diffraction data are gathered in Table 4. For both models the refined magnetic moments are close to the 7 μ_B expected for Eu^{2+} ions. The planar orientation of the Eu^{2+} magnetic moments combined with the q_x component of the propagation vector results in a flat spiral magnetic structure[63] (Fig. 16). In order to confirm that all of the magnetic diffraction peaks (even those of weak intensity or at same 2-theta angles as nuclear Bragg peaks) are perfectly refined using this flat spiral magnetic structure, a difference pattern between neutron diffraction data recorded in the magnetically ordered state (T = 5.5 K) and in the paramagnetic state (T = 20 K) at a wavelength of λ = 1.3286 Å shown in Fig. 17.

The flat spiral magnetic structure, shown in Fig. 16, is characterized by the rotation of the Eu magnetic moments in the (b, c) plane with the rotation angle Φ_i (in degrees) calculated

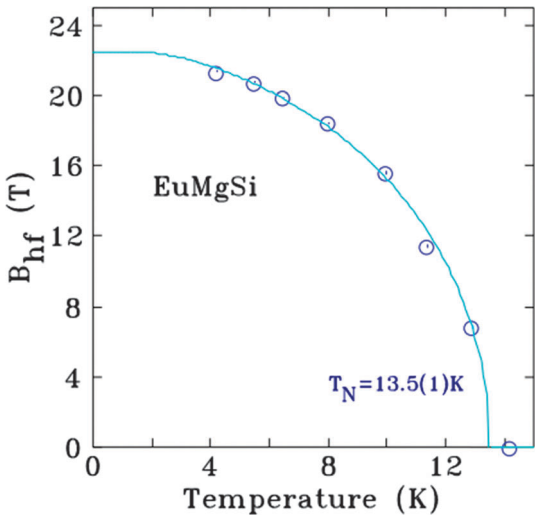

Fig. 11 Temperature dependence of the magnetic hyperfine fields of the ^{151}Eu Mössbauer spectra of EuMgSi. The continuous line represents a least-squares fit with an S = 7/2 Brillouin function.

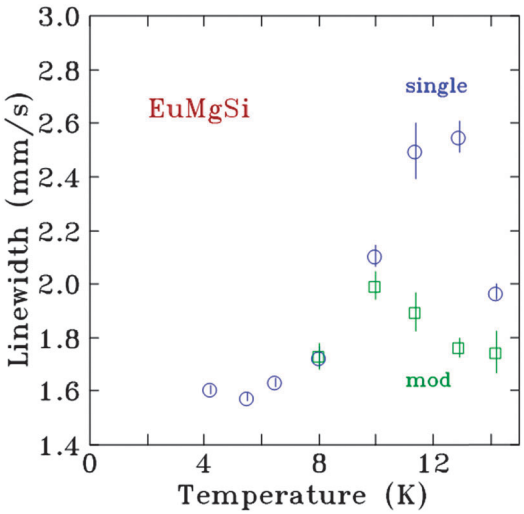

Fig. 12 Fitted linewidths of the ^{151}Eu Mössbauer spectra of EuMgSi as a function of temperature. Blue circles denote fits with single europium sites and the green squares refer to the fits including the modulation. For details see the text.

from the relation $\Phi_i = (x_i \times q_x + \alpha_i) \times 360$, where x_i is the x coordinate of the ith atom, q_x is the x component of the propagation vector k and α_i is the magnetic phase angle of the atom being considered. Thus, in the first crystallographic cell (i = 1), Eu(1), Eu(2), Eu(3), and Eu(4) have rotation angles of 2°, 163°, 97°, and 69°, respectively. From one crystallographic cell to the next, the magnetic moment of a particular Eu atom (*e.g.* Eu(1)) rotates by $q_x \times 360 = 133.2°$.

In the TiNiSi-type structure, the principal Eu–Eu magnetic couplings occur between the Eu(1) and Eu(2) atoms ($d_{Eu(1)-Eu(2)}$ = 379.6 pm for EuMgSi at 5.5 K), which form zigzag chains along the b-axis (Fig. 1), and between the Eu(1) and Eu(4) atoms ($d_{Eu(1)-Eu(4)}$ = 400.2 pm for EuMgSi at 5.5 K), which form zigzag

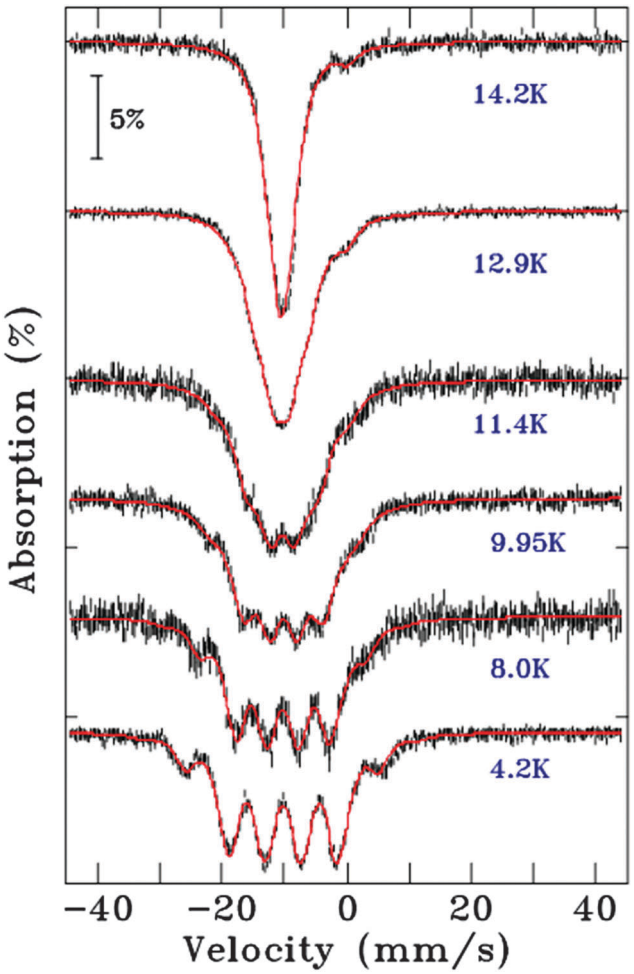

Fig. 13 ^{151}Eu Mössbauer spectra of EuMgSi fitted with the incommensurate modulation model.[46]

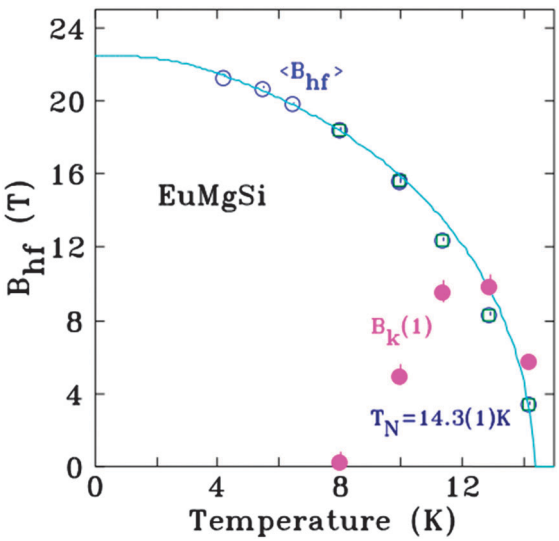

Fig. 14 Temperature dependence of the magnetic hyperfine fields of the ^{151}Eu Mössbauer spectra of EuMgSi as obtained from the fits with the incommensurate model. The magnitude of the sinusoidal modulation term B_k(1) is plotted in magenta.

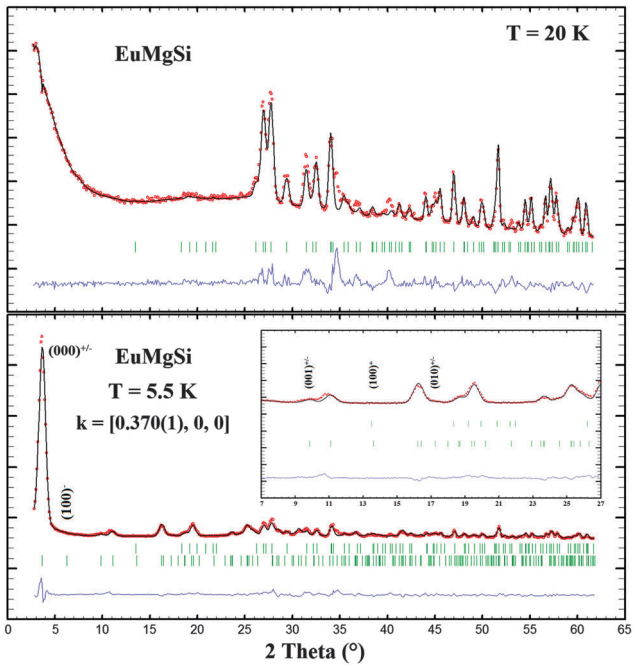

Fig. 15 Experimental and refined neutron diffraction patterns of EuMgSi at 20 K (top) and 5.5 K (bottom) at a wavelength of λ = 1.3286 Å.

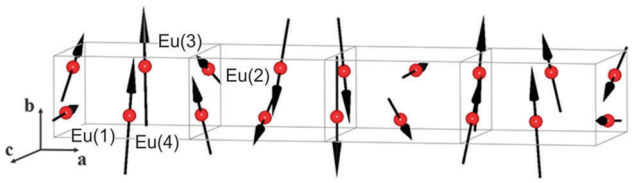

Fig. 16 The flat spiral magnetic structure of EuMgSi at T = 5.5 K. For clarity, the non-magnetic Mg and Si atoms were omitted.

Table 4 Results from the various refinements of the 5.5 K neutron diffraction pattern of EuMgSi

	Helimagnetic 1	Helimagnetic 2
a/pm	767.5(4)	767.6(3)
b/pm	453.4(2)	453.5(2)
c/pm	834.1(3)	834.0(3)
V/nm^3	0.2902(2)	0.2903(2)
q_x	0.370(1)	0.370(1)
θ_C/°	90	90
θ/°	90	90
Φ/°	0	0
Magn. Phases	0; 0; 0; 0	0; 0.09(1); 0.09(1); 0
μ_{Eu}/μ_B	6.49(9)	6.74(10)
R(Bragg); R(f)	22.0; 17.4	22.2; 17.6
R(Magn.)	11.3	10.6
R(wp); R(exp.)	10.1; 1.46	9.59; 1.46
χ^2	47.8	43.4

chains along the a-axis (Fig. 1). At 5.5 K, the Eu(1)–Eu(4) and Eu(2)–Eu(3) magnetic interactions comprise both ferro- and antiferromagnetic couplings (Fig. 16) arising from the q_x component of the propagation vector of 0.370. The Eu(1)–Eu(2) and Eu(3)–Eu(4) magnetic couplings comprise also both ferro- and

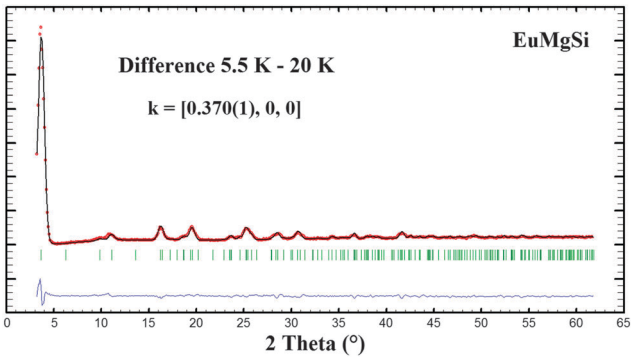

Fig. 17 Flat spiral magnetic structure fit to the difference pattern between 5.5 K and 20 K with ΦEu(1) = ΦEu(4) = 0 and ΦEu(2) = ΦEu(3) = 0.09 (λ = 1.3286 Å).

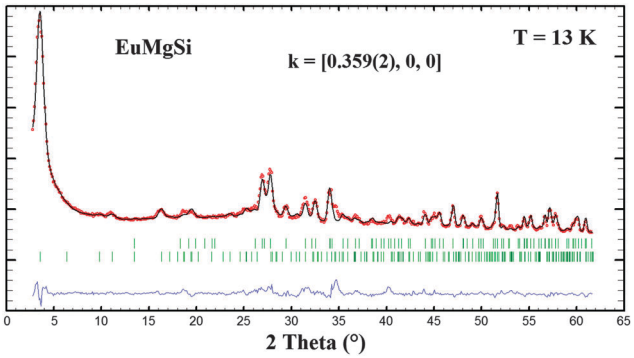

Fig. 18 The alternative flat spiral magnetic structure fit to the 13 K pattern (λ = 1.3286 Å).

antiferromagnetic contributions (Fig. 16) due to both the non-zero q_x component of the propagation vector and the different magnetic phase angles between Eu(1) and Eu(2), and between Eu(3) and Eu(4).

In order to look for changes in the magnetic structure between the two ordering temperatures identified by both susceptibility and heat capacity, a long-duration neutron diffraction pattern was recorded at T = 13 K. Examination of the data and comparison of the difference patterns (5.5–20 K and 13–20 K) revealed no significant changes beyond the expected reduction in overall magnetic intensity. The strong similarities between the patterns recorded at 13 K and 5.5 K indicate that any change in the magnetic structure is quite small. Fig. 18 shows the 13 K diffraction pattern fitted with the same flat spiral magnetic structure used to fit the T = 5.5 K data shown in Fig. 15. This refinement leads to propagation vector k = [$q_x \approx$ 0.36, 0, 0], magnetic phase angles of 0.10(2) for Eu(2) and Eu(3) atoms (the magnetic phase angles of Eu(1) and Eu(4) atoms are kept zero) and a europium magnetic moment of 3.07(6) μ_B. Only a weak difference between the neutron patterns is observed in the intensity of the magnetic peak at 2Θ = 18.7°. Its intensity is comparable to that of the magnetic peak at 2Θ = 16.3° at 13 K but somewhat lower at 5.5 K. Unfortunately, due to the overall weakness of the observed changes in the magnetic diffraction peaks, the fact that three overlapping magnetic reflections

contribute to the peak at $2\Theta = 18.7^\circ$, and the significant reduction in the background at a low angle ($2\Theta < 25^\circ$) due to magnetic ordering, it is not possible to comment further on possible changes to the magnetic structure at 12 K solely on the basis of our neutron diffraction data. Possible explanations of this intensity modification of the above mentioned magnetic peaks are still under consideration. One of them is a statistic orientation within the *b*, *c*-plane after the first magnetic anomaly, which would be consistent with the 13 K diffraction pattern. However, in this case we would expect dynamic processes that we do not observe in the ac-susceptibility.

Conclusions

We find that no structural change takes place down to liquid helium temperatures for Zintl phase EuMgSi, which is known to crystallize in the TiNiSi-type structure. No changes in lattice parameters due to magnetic ordering phenomena are observed. Investigations of the magnetic properties by dc- and ac-susceptibility measurements clearly prove two different magnetic anomalies around 12 and 14 K. By investigation of the heat capacity and the resistivity both anomalies are confirmed and their intrinsic character is as well be underlined by ^{151}Eu Mössbauer spectroscopy. Consistently, resistivity measurements and DFT calculations identify EuMgSi as a nearly zero gap semiconductor. A small band gap energy of approximately 0.03 eV could be obtained from the resistivity measurement. With reference to the dc- and ac-susceptibility investigations we could identify evidence for antiferromagnetic as well as ferromagnetic interactions. The contributions of both types of interactions to magnetism are nicely proven by neutron diffraction due to the non-zero q_x component. Below both transitions we were able to solve an incommensurate magnetic structure with the propagation vector $k = [q_x \approx 0.37, 0, 0]$. Unfortunately, no second magnetic structure could be identified most likely due the small temperature gap between the ordering temperatures. We will continue with investigations of the isotypic EuCdGe which may reveal additional insights into these delicate magnetic systems.

Acknowledgements

This work was supported by the Deutsche Forschungsgemeinschaft. O. N. is indebted to the NRW Forschungsschule *Molecules and Materials – A Common Design Principle* for a PhD fellowship.

References

1 D. Panke and E. Wölfel, *Z. Kristallogr.*, 1968, **129**, 9–28.
2 P. Eckerlin and E. Wölfel, *Z. Anorg. Allg. Chem.*, 1955, **280**, 321–331.
3 A. Widera, B. Eisenmann and H. Schäfer, *Z. Naturforsch.*, 1976, **31b**, 520–521.
4 A. Widera and H. Schäfer, *Z. Naturforsch.*, 1976, **31b**, 1434–1435.
5 G. Busch, P. Junod, U. Katz and U. Winkler, *Helv. Phys. Acta*, 1954, **27**, 193–195.
6 V. E. Borisenko, Fundamental Electric Properties of Semiconducting Silicides, in *Silicides–Fundamentals and Applications*, Proceedings of the 16th Course of the International School of Solid State Physics, Erice, Italy, 5–16 June 1999, ed. L. Miglio and F. d'Heurle, World Scientific, Singapore, 2000, pp. 108–125.
7 B. Yu, D. Chen, Q. Tang, C. Wang and D. Shi, *J. Phys. Chem. Solids*, 2010, **71**, 758–763.
8 J. Hu, A. Kato, T. Sadoh, Y. Maeda, K. N. Galkin, T. V. Turchin and H. Tatsuoka, *Int. J. Mod. Phys. B*, 2010, **24**, 3693–3699.
9 H. Ihou-Mouko, C. Mercier, J. Tobola, G. Pont and H. Scherrer, *J. Alloys Compd.*, 2011, **509**, 6503–6508.
10 Y. Katsura and H. Takagi, *J. Electron. Mater.*, 2013, **42**, 1365–1368.
11 R. Mishra, R.-D. Hoffmann, R. Pöttgen, H. Trill and B. D. Mosel, *Z. Anorg. Allg. Chem.*, 2002, **628**, 741–744.
12 A. Palenzona, P. Manfrinetti, S. Brutti and G. Balducci, *J. Alloys Compd.*, 2003, **348**, 100–104.
13 H. Axel, B. Eisenmann, H. Schäfer and A. Weiss, *Z. Naturforsch.*, 1969, **24b**, 815–817.
14 O. F. Zmiy, *Visn. Lviv Derzh. Univ., Ser. Khim.*, 1971, **12**, 5–7.
15 B. Eisenmann, H. Schäfer and A. Weiss, *Z. Anorg. Allg. Chem.*, 1972, **391**, 241–254.
16 H. Wu, W. Zhou, T. J. Udovic and J. J. Rush, *J. Alloys Compd.*, 2007, **446–447**, 101–105.
17 J. B. Whalen, J. V. Zaikina, R. Achey, R. Stillwell, H. Zhou, C. R. Wiebe and S. E. Latturner, *Chem. Mater.*, 2010, **22**, 1846–1853.
18 F. Merlo, M. Pani and M. L. Fornasini, *J. Alloys Compd.*, 1993, **196**, 145–148.
19 Y. Niwa, Y. Todaka, T. Masuda, T. Kawai and M. Uemoto, *Mater. Trans., JIM*, 2009, **50**, 1725–1729.
20 K. Hagihara, K. Fujii, A. Matsugaki and T. Nakano, *Mater. Sci. Eng., C*, 2013, **33**, 4101–4111.
21 R. Pöttgen and D. Johrendt, *Chem. Mater.*, 2000, **12**, 875–897.
22 R. Pöttgen, *Z. Kristallogr.*, 1996, **211**, 884–890.
23 D. Johrendt, G. Kotzyba, H. Trill, B. D. Mosel, H. Eckert, Th. Fickenscher and R. Pöttgen, *J. Solid State Chem.*, 2002, **164**, 201–209.
24 L. Li, O. Niehaus, B. Gerke and R. Pöttgen, *IEEE Trans. Magn.*, 2014, **50**, 2503604 (4pp).
25 A. Slabon, E. Cuervo-Reyes, O. Niehaus, F. Winter, C. Mensing, R. Pöttgen and R. Nesper, *Z. Anorg. Allg. Chem.*, 2014, **640**, 1861–1867.
26 D. H. Ryan and L. M. D. Cranswick, *J. Appl. Crystallogr.*, 2008, **41**, 198–205.
27 D. Kußmann, R.-D. Hoffmann and R. Pöttgen, *Z. Anorg. Allg. Chem.*, 1998, **624**, 1727–1735.
28 K. Yvon, W. Jeitschko and E. Parthé, *J. Appl. Crystallogr.*, 1977, **10**, 73–74.
29 A. P. Hammersley, S. O. Svensson, M. Hanfland, A. N. Fitch and D. Hausermann, *High Pressure Res.*, 1996, **14**, 235–248.

30 J. Rodriguez-Carvajal, *Physica B*, 1993, **192**, 55–69.
31 T. Roisnel and J. Rodriguez-Carvajal, *Mater. Sci. Forum*, 2001, **378–381**, 118–123.
32 L. Palatinus and G. Chapuis, *J. Appl. Crystallogr.*, 2007, **40**, 786–790.
33 V. Petříček, M. Dušek and L. Palatinus, *Z. Kristallogr.*, 2014, **229**, 345–352.
34 S. J. Clark, M. D. Segall, C. J. Pickard, P. J. Hasnip, M. I. J. Probert, K. Refson and M. C. Payne, *Z. Kristallogr.*, 2005, **220**, 567–570.
35 B. Delley, *J. Chem. Phys.*, 2000, **113**, 7756–7764.
36 O. K. Andersen and O. Jepsen, *The Stuttgart Tight-Binding LMTO-ASA program Version 4.7*, Max-Planck-Institut für Festkörperforschung. Heisenbergstrasse 1, D-70569 Stuttgart, Germany, 1998.
37 J. P. Perdew, K. Burke and M. Erzenhof, *Phys. Rev. Lett.*, 1996, **77**, 3865–3868.
38 T. Ziegler, *Chem. Rev.*, 1991, **91**, 651–667.
39 D. C. Langreth and M. J. Mehl, *Phys. Rev. Lett.*, 1981, **47**, 446–450.
40 E. Cuervo Reyes, A. Slabon-Turski, C. Mensing and R. Nesper, *J. Phys. Chem. C*, 2012, **116**, 1158–1164.
41 A. Savin, A. D. Becke, J. Flad, R. Nesper, H. Preuss and H. G. von Schnering, *Angew. Chem., Int. Ed. Engl.*, 1991, **30**, 409–412.
42 A. Savin, R. Nesper, S. Wengert and T. F. Fässler, *Angew. Chem., Int. Ed. Engl.*, 1997, **36**, 1808–1832.
43 L. J. van der Pauw, *Philips Res. Rep.*, 1958, **13**, 1–9.
44 D. R. Lide, *Handbook of Chemistry and Physics*, CRC Press, New York, 75th edn, 1996–1997, pp. 11–41.
45 R. A. Brand, *Normos Mössbauer fitting Program*, Universität Duisburg, Duisburg, Germany, 2007.
46 A. Maurya, P. Bonville, A. Thamizhavel and S. K. Dahr, *J. Phys.: Condens. Matter*, 2014, **26**, 216001 (10 pp).
47 R.-D. Hoffmann and R. Pöttgen, *Z. Kristallogr.*, 2001, **216**, 127–145.
48 G. Nuspl, K. Polborn, J. Evers, G. A. Landrum and R. Hoffmann, *Inorg. Chem.*, 1996, **35**, 6922–6932.
49 G. A. Landrum, R. Hoffmann, J. Evers and H. Boysen, *Inorg. Chem.*, 1998, **37**, 5754–5763.
50 E. Parthé, L. Gelato, B. Chabot, M. Penzo, K. Cenzual and R. Gladyshevskii, *TYPIX-Standardized Data and Crystal Chemical Characterization of Inorganic Structure Types. Gmelin Handbook of Inorganic and Organometallic Chemistry*, Springer, Berlin, Germany, 8th edn, 1993.
51 M. D. Bojin and R. Hoffmann, *Helv. Chim. Acta*, 2003, **86**, 1653–1682.
52 J. Emsley, *The Elements*, Oxford University Press, Oxford, UK, 1999.
53 M. K. Wilkinson, J. W. Cable, E. O. Wollan and W. C. Koehler, *Phys. Rev.*, 1959, **113**, 497–507.
54 X. Ma, J. Lu, J. B. Whalen and S. E. Latturner, *Inorg. Chem.*, 2013, **52**, 3342–3348.
55 J. A. Mydosh, *J. Magn. Magn. Mater.*, 1996, **157/158**, 606–610.
56 K. Łątka, R. Kmieć, J. Gurgul, A. W. Pacyna, M. Rams, T. Schmidt and R. Pöttgen, *J. Magn. Magn. Mater.*, 2006, **301**, 359–370.
57 R. L. Carlin, *Magnetochemistry*, Springer-Verlag, Berlin, NY, 1986.
58 K. Łątka, R. Kmieć, A. W. Pacyna, R. Mishra and R. Pöttgen, *Solid State Sci.*, 2001, **3**, 545–558.
59 C. Michel, S. D. Baranovskii, P. J. Klar and P. Thomas, *Appl. Phys. Lett.*, 2006, **89**, 112116 (3pp).
60 R. Srivastava, *J. Sens. Technol.*, 2012, **2**, 8–12.
61 P. Lemoine, J. M. Cadogan, D. H. Ryan and M. Giovannini, *J. Phys.: Condens. Matter*, 2012, **24**, 236004 (8pp).
62 D. H. Ryan, A. Legros, O. Niehaus, R. Pöttgen, J. M. Cadogan and R. Flacau, *J. Appl. Phys.*, 2015, **117**, 17D108 (5 pp).
63 J. Rodriguez-Carvajal and F. Bourée, *EPJ Web Conf.*, 2012, **22**, 00010 (52 pp).